Neutron microtomography to investigate the bone-implant interface – comparison with histological analysis

Florian Guillaume, Sophie Le Cann, Alessandro Tengattini, Elin Törnquist, Céline Falentin-Daudre, Hugues Albini-Lomami, Yvan Petit, Hanna Isaksson, Guillaume Haiat

Neutron microtomography to investigate the bone-implant interface – comparison with histological analysis

Florian Guillaume[1,2], Sophie Le Cann[2], Alessandro Tengattini[3,4], Elin Törnquist[5], Céline Falentin-Daudre[6], Hugues Albini Lomami[2], Yvan Petit[1], Hanna Isaksson[5] and Guillaume Haïat[2*]

[1] Département de génie mécanique, École de technologie supérieure, Montréal, Canada
[2] MSME, CNRS UMR 8208, Univ Paris Est Creteil, Univ Gustave Eiffel, F-94010 Creteil, France
[3] Institut Laue Langevin, Grenoble, France
[4] Laboratoire 3SR, Université Grenoble Alpes, Gières, France
[5] Department of Biomedical Engineering, Lund University, 221 00 Lund, Sweden
[6] LBPS/CSPBAT, UMR CNRS 7244, Institut Galilée, Université Sorbonne Paris Nord, 99 avenue JB Clément 93430 Villetaneuse, France

*E-mail: guillaume.haiat@cnrs.fr

Abstract

Bone properties and especially its microstructure around implants are crucial to evaluate the osseointegration of prostheses in orthopaedic, maxillofacial and dental surgeries. Given the intrinsic heterogeneous nature of the bone microstructure, an ideal probing tool to understand and quantify bone formation must be spatially resolved. X-ray imaging has often been employed, but is limited in the presence of metallic implants, where severe artefacts generally arise from the high attenuation of metals to X-rays. Neutron tomography has recently been proposed as a promising technique to study bone-implant interfaces, thanks to its lower interaction with metals. The aim of this study is to assess the potential of neutron tomography for the characterisation of bone tissue in the vicinity of a metallic implant. A standardised implant with a bone chamber was implanted in rabbit bone. Four specimens were imaged with neutron tomography and subsequently compared to non-decalcified histology to stain soft and mineralised bone tissues, used here as a ground-truth reference. An intensity-based image registration procedure was performed to place the 12 histological slices within the corresponding 3D neutron volume. Significant correlations ($p < 0.01$) were obtained between the two modalities for the bone-implant contact (*BIC*) ratio ($R = 0.77$) and the bone content inside the chamber ($R = 0.89$). The results indicate that mineralised bone tissue can be reliably detected by neutron tomography. However, the *BIC* ratio and bone content were found to be overestimated with neutron imaging, which may be explained by its sensitivity to non-mineralised soft tissues, as revealed by histological staining. This study highlights the suitability of neutron tomography for the analysis of the bone-implant interface. Future work will focus on further distinguishing soft tissues from bone tissue, which could be aided by the adoption of contrast agents.

Keywords: neutron tomography, titanium implant, osseointegration, histological staining, image registration

1. Introduction

Metal implants are widely employed in orthopaedic, maxillofacial and dental surgeries, to repair damaged joints, bones or teeth. Despite their widespread clinical use, implant failures still occur (Eskelinen et al., 2006; Moy et al., 2005; Sharkey et al., 2014), with dramatic consequences (Kurtz et al., 2014, 2007). The success of the surgical intervention is measured by the implant long-term stability (Haïat et al., 2014). This is controlled by osseointegration, which corresponds to bone healing and growing onto and around the implant, creating a solid bone-implant interface (Shemtov-Yona and Rittel, 2015). A better understanding of the bone-implant interface development and the evolution of its biomechanical properties – such as bone tissue composition, quantity and structure – is pivotal for a more reliable prediction of the surgical outcome (Winter et al., 2004).

The evolution of bone-implant interface properties is difficult to study systematically because of the variability in the implant characteristics used in clinical practice. To overcome this issue, standardised implant models have been developed, such as a coin-shaped implant, previously used to demonstrate the influence of implant roughness (Rønold et al., 2003; Rønold and Ellingsen, 2002) and healing time (Mathieu et al., 2012) on osseointegration phenomena. To further investigate local variations in the bone-implant interface formation, this reference coin-shaped implant model has been modified by our group to include a bone chamber which allow a clear distinction between mature and newly formed bone tissues. Adopting this implant model, it was possible to explore the spatiotemporal variations of the mechanical (Fraulob et al., 2020a; Mathieu et al., 2011; Vayron et al., 2011, 2012, 2014), structural (Le Cann et al., 2020) and compositional properties (Fraulob et al., 2020b) of bone.

In addition to bone quality, bone quantity and microstructure in the vicinity of the implant are crucial parameters influencing the implant stability (Wirth et al., 2011). Histological analysis is generally considered the gold standard approach when trying to retrieve such information at the bone-implant interface (Jackson et al., 2019). Notably, histological analysis has been used to identify the different types of bone tissues and cells around implants (Berglundh et al., 2003) and to measure the bone-implant contact ratio (*BIC*), a key parameter to evaluate the quality of the osseointegration (Berglundh et al., 2003; Jimbo et al., 2013). However, the histological analysis approach presents some important drawbacks as it is destructive, 2D and limits the analysis of the bone-implant interface to a reduced number of slices, significantly increasing the risk of neglecting important variations in structure and *BIC* ratio (up to 30% difference between sequential slices (Neldam et al., 2017)).

Given its non-destructive and 3D nature, X-ray computed microtomography has started to become a reference technique to evaluate bone microstructural properties (Burghardt et al., 2011), and has been used to access the 3D bone network around implants (Bissinger et al., 2017; De Smet et al., 2006; Gielkens et al., 2008; Palmquist, 2018). Nonetheless, given the interaction of X-rays with the electron cloud of atoms, the large difference of attenuation between the low density, low atomic number elements within biological tissues (or air) and the heavier elements comprised in metal implants generally induces severe "streaking" artefacts in x-ray tomography (Li et al., 2014). These artefacts are more pronounced in the proximity of the metal, *i.e.* at their interface with bone, and are difficult to rigorously remove from the images, hindering the analysis of bone-implant interface (Kovacs et al., 2018; Treece, 2017).

Interacting with the nucleus of atoms, neutrons are more sensitive to light atoms like hydrogen, while being rather insensitive to metals (Schwarz et al., 2005), thus provide a different and highly complementary contrast as compared to X-rays. Neutron tomography has been applied to several fields (Kardjilov et al., 2018) such as geomechanics (Tengattini et al., 2021) and materials sciences. Because neutrons have minimal influence on the structural integrity of matter (Burca et al., 2018), neutron tomography represents a good probe for imaging biological specimens, and has been used to investigate structure and composition of pearls (Micieli et al., 2018) and fossils (Schwarz et al., 2005; Urciuoli et al., 2018). In biomechanics, the technique has only recently been applied to study the bone-implant interface, proving its ability to reduce artefacts around metallic implants in contrast to X-ray tomography (Isaksson et al., 2017). This technique was also employed to investigate the mechanical properties of the bone-implant interface *via in-situ* pull-out tests analysed through digital volume correlation (Le Cann et al., 2017). Qualitative comparison of neutron tomography to histology was conducted in the context of lung tissues (Cekanova et al., 2014; Watkin et al., 2009). However, there is, to date, no quantitative and detailed comparison between histology and neutron tomography to study the bone-implant interface.

To rigorously compare the outcome of two different imaging modalities, it is essential to register (*i.e.* spatially align) the two measurements (*i.e.* images) so as to directly compare the values of the individual pixels as well as the indexes of a region. In life sciences, image registration has been employed to help the understanding of tissues morphology and behavior, such as blood vessel structure (McLaughlin et al., 2005) and bone growth (Stalder et al., 2014), based on the comparison, for example, of X-ray tomography scans and histology (Meagher et al., 2017; Stalder et al., 2014), or MRI scans and X-ray radiography (McLaughlin et al., 2005). Two main methods have generally been employed for image registration in the literature (Markelj et al., 2012): feature-based registration – which aims at reducing the distance between specific features (points, curves or surfaces) of segmented images – and intensity-based registration – which focuses on matching pixels by minimising a potential based on their grey value. Intensity-based registration has been shown to be more accurate (Henke et al., 2019; McLaughlin et al., 2005), especially when using

segmented images (Markelj et al., 2012; Turgeon et al., 2005; Vermandel et al., 2007). This image registration technique has successfully been applied in various fields, such as in brain surgery combining X-ray with MRI images (McLaughlin et al., 2005; Vermandel et al., 2007), in cardiology with angiograms and a 3D patient-specific heart model (Turgeon et al., 2005), and in plant biology where fluorescence images were registered to visible light images (Henke et al., 2019). However, such approach has not been applied so far to neutron tomography in the context of implant osseointegration.

This study compares the performances of neutron tomography and histology on the bone-implant interface properties, to assess the reliability of the neutron tomography approach as compared to the ground truth provided by histology. Adopting the aforementioned bone chamber model, the *BIC* ratio and the amount of bone tissue present in the bone chamber were specifically compared between modalities after using intensity-based image registration to locate the histological slices in the corresponding neutron volume images.

2. Material & methods

2.1 Implants and surgical procedure

One New Zealand White rabbit (6 months, weight around 4 kg) was implanted with four Ti6Al4V coin-shaped implants (5 mm in diameter, 3 mm in height), on both distal femurs and proximal tibiae. Implants were polished using #1200 SiC abrasive papers (LabPol-5, Struers®, Ballerup, Denmark) before being placed *in vivo*. The surgical procedure is detailed in (Vayron et al., 2014). In short, each implant was surrounded by a PTFE cap in order to create a 200 µm-thick bone chamber between the implant and the bone, which was maintained for twelve weeks of healing time thanks to orthodontic elastic strings and osteosynthesis screws (figure 1a). Animal handling was approved by the ethical committee of ENVA (École Nationale Vétérinaire d'Alfort), and the rabbit was housed following the European guidelines for care and use of laboratory animals (19°C, humidity 55%, food and water *ad libitum*). After euthanasia, femurs and tibiae were extracted, and the bone-implant interface with surrounding tissues was isolated by drilling 9 mm diameter cores (about 6 mm in height) around the implants, performed at low speed and under constant irrigation with saline solution (figure 1b). Specimens were stored in absolute ethanol at 4°C.

2.2 Neutron tomography

The four specimen cores were imaged with neutron tomography at the NeXT beamline at the Institut Laue Langevin, Grenoble, France (Tengattini et al., 2020). To avoid undesirable variations during the tomographies (notably through water evaporation, which is highly visible to neutrons) and to maximise image quality and contrast, specimens were left to dry at 4°C for up to 10 hours. The specimens were then piled up in groups of two inside a custom-made, sealed Teflon sample holder. Each set was imaged with a neutron flux of 9.10^7 neutrons.cm^{-2}.s^{-1} with an isotropic voxel size of 7.5 µm, field of view 13.5 x 13.5 mm², using 1792 projections over 360° rotation. Each projection had an exposure time of 7 s and was averaged 3 times, resulting in a 10.5h scan. From these projections, the 3D volumes were reconstructed with a Feldkamp reconstruction algorithm with identical parameters, adopting the commercial reconstruction software X-Act (RX Solutions®, Chanavod, France) (figure 1c).

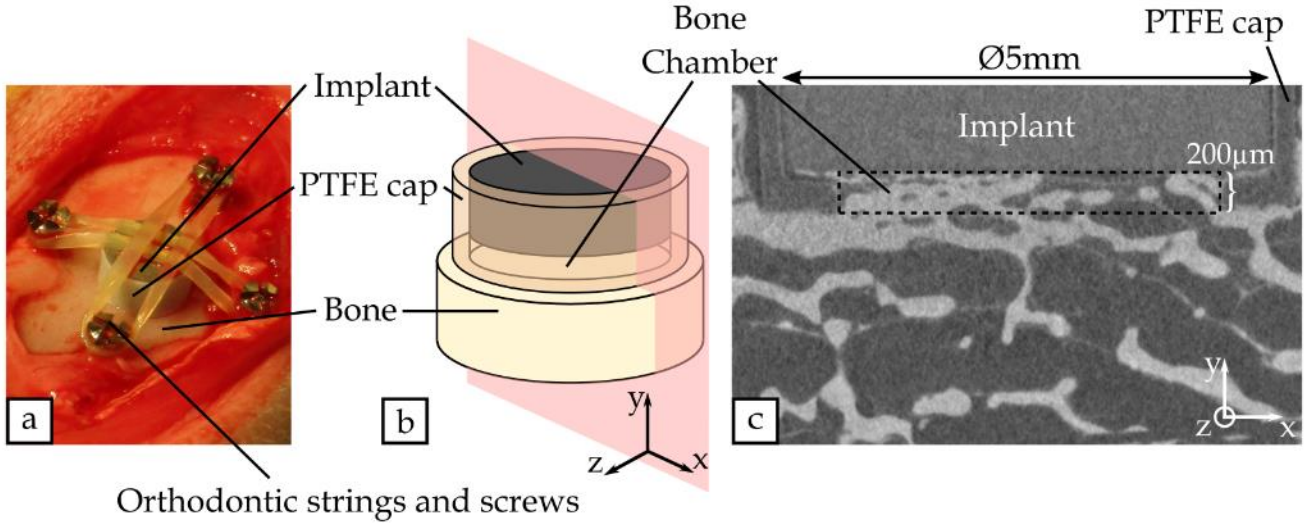

Figure 1: Implant model. (a) Photography of the implant model during implantation surgery, on a rabbit tibia. (b) Schematic representation of a specimen after sacrifice. (c) Representative vertical 2D cross-section of a neutron tomography volume (as schematized in red in (b)).

2.3 Histology

After imaging, the specimens were fixed in 10% formalin for one week and dehydrated in successive 24-hours baths with increasing concentration of ethanol (70°, 80°, 90° and 100°) and 1 h vacuum periods to remove air bubbles. Specimens were then cleared in xylene and directly embedded in PMMA (Chevallier et al., 2010; Soffer et al., 2006). Three 400 µm-thick slices were cut in the middle of each specimen, perpendicularly to the bone-implant interface (XY plane, as per orientation in figure 1b), with a low-speed cutting machine (Minitom, Struers®, Ballerup, Denmark) under constant water irrigation. Slices were polished using #1200 and #2000 SiC abrasive papers (LabPol-5, Struers®, Ballerup, Denmark) followed by polishing cloths with alumina suspensions of 9 µm and 0.3 µm grain size. Non-decalcified histology was performed with van Gieson picro-fuchsin to stain mineralised tissues with a maximum penetration depth of 15 µm (data not shown), followed by Stevenel's blue staining to reveal non-mineralised soft tissues. All slices were analysed under standard light microscopy (Stemi 305, Zeiss, China) (pixel size 2.3 µm).

2.4 Image analysis

2.4.1 Pre-processing of neutron images. Neutron tomography image volumes were reduced to 8-bit to limit calculation time during registration and filtered using a 3D Mean filter (r=2 pixels) (Ollion et al., 2013), implemented within the Fiji software (Schindelin et al., 2012) in order to increase the signal-to-noise ratio. All image volumes were manually rotated to align the bone-implant interface with the XZ plane (TransformJ plugin (Meijering et al., 2001)). For each image volume, bone tissue was segmented based on a specimen-specific threshold interval. The lower boundary was chosen based on the median of all the thresholds obtained from each XZ image of the image volume through the IsoData method (Ridler and Calvard, 1978) (134 ± 3, 8-bit images). The upper boundary to remove brighter areas in the images was chosen based on a visual inspection (190). After segmentation, any remaining noise was minimised by applying combinations of binary erosions and dilations (Open and Close) in each direction of space (r=1 pixel). The implant was not visible in the segmented images because its grey values were below the segmentation threshold.

2.4.2 Pre-processing of histological slices. Van Gieson stained histological slices were colour-filtered using red and green filters to isolate bone tissue from the implant through manual segmentation (Fiji software). Again, two binary operations (Open and Close) were carried out to remove the remaining noise in the images.

2.4.3 Image registration procedure. An image registration procedure was conducted for all 12 histological images to determine the corresponding 2D section of 3D neutron volume (figure 2). This registration was performed in Matlab (R2017b, MathWorks Inc., MA, USA) adopting an intensity-based registration method (Henke et al., 2019). A subset of the neutron volume indicatively matching the segmented histology image was pre-selected based on visual inspection. Each segmented histological image was pre-downscaled to match approximately the pixel size of the neutron image (7.5 µm). The registration approach minimises a "similitude potential" between the images acquired with the two modalities, based on a scalar value named "*Fit*" and calculated as:

$$Fit = Fit_H + Fit_N$$

$$Fit = \frac{Card(Bone_N \cap Bone_H)}{Card(Bone_H)} + \frac{Card(Bone_N \cap Bone_H)}{Card(Bone_N)}$$

where $Bone_N$ and $Bone_H$ represent the segmented pixels corresponding to bone in the neutron tomography image and in the histological image, respectively. The parameter *Fit* is the sum of two modality-specific parameters, Fit_H and Fit_N, each of which evaluates the extent of overlap of segmented pixels in one modality as compared to the other. For instance, a Fit_H value of 100% indicates that the whole histological image is found in the neutron image. The registration algorithm iteratively maximises this similitude potential, by varying the relative position of the two images, conducted *via* translation (along the X and Y axes), rotation (around the Z axis) as well as scaling (within a 2% limit) of the segmented histological slice, to match the selected segmented neutron images (see Registration step in figure 2). Subsequently, a second step iteratively improves the orientation and position of the selected neutron slice (rotation along the X and Y axes, and translation along the Z axis), in order to identify the neutron image that best matched the histological image. For all specimens, the registration procedure was iterated until the rotation to be applied to the neutron image volume was under ± 0.2° (X and Y axes), with an image positioning error (Z axis) of ± 1 image (pixel size 7.5 µm).

2.4.4 Comparison of histology and neutron tomography. After the image registration detailed above, the selected neutron image was quantitatively compared to its histological reference image by calculating two key indicators of both modalities: the bone-implant contact ratio (*BIC*) and the bone content within the bone chamber. The *BIC* ratio within the chamber was measured on a line at the bone-implant interface, and defined as the number of segmented bone pixels ($Bone_H$ and $Bone_N$) divided by the total number of pixels corresponding to the chamber width. Bone content was calculated as the ratio between the number of bone pixels and the total number of pixels inside the bone chamber. A visual comparison between the registered neutron image and its histological reference image stained with Stevenel's blue was also performed.

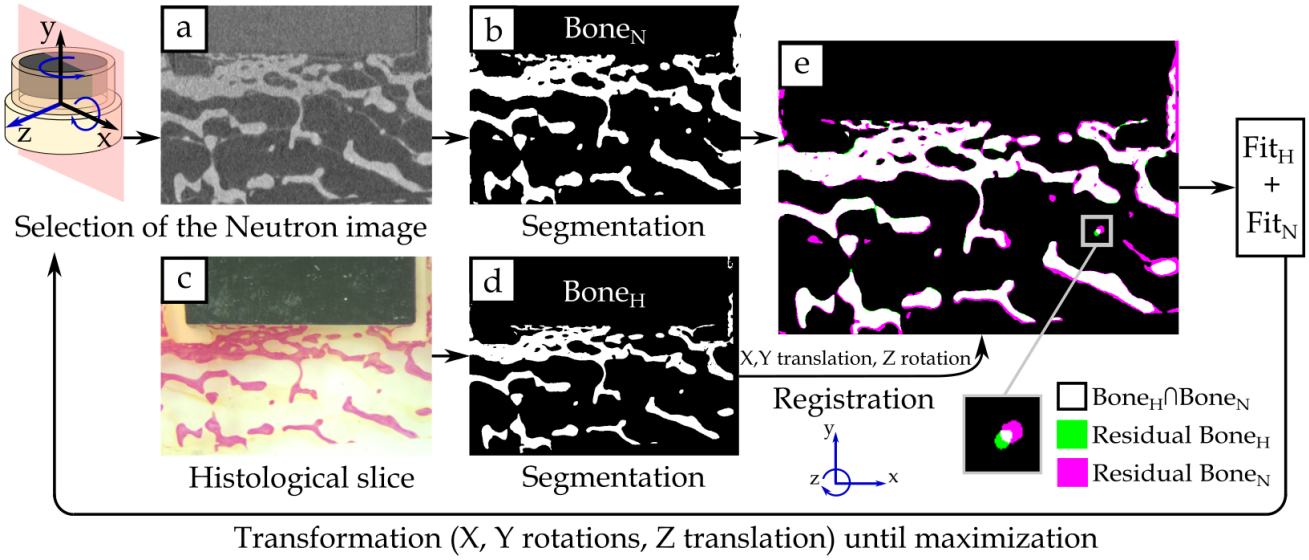

Figure 2: Illustration of the image registration procedure adopted to identify and register the neutron image corresponding to the histological slice. A 2D image of the neutron tomography was selected (a) and segmented (*Bone$_N$*) (b). In parallel, the histological slice (c) was also segmented (*Bone$_H$*) (d) and registered to the segmented neutron images (e) by minimising a similitude potential, varying the X-Y position, the Z-rotation and scale of the histological image. In the registered image (e), the colour code highlights the differences in the segmented bone pixels: in white the pixels present simultaneously in the neutron (b) and the histological (d) images, in green remaining bone pixels left in the histological image (*Residual Bone$_H$*) and in fuchsia the ones left in the neutron image (*Residual Bone$_N$*). The two fit ratios (*Fit$_H$* and *Fit$_N$*) were computed for each registration step. A second loop optimised the selection of the neutron slice by rotating the neutron volume around the X and Y axes, and translating it along the Z axis. The procedure ended when a stable maximum of the sum of *Fit$_N$* and *Fit$_H$* was reached.

2.5 Statistical analysis

The *BIC* ratio and the bone content values were compared between the two techniques using linear regression analyses by determining the Pearson's correlation coefficient (*R*). Normal distribution was evaluated with a Shapiro-Wilk test at a significance level of $p = 0.05$. Calculations were performed using R software (R Development Core Team, 2005).

3. Results

Intensity-based registration was successfully performed on all the 12 histological slices, identifying their corresponding neutron slices.

Results are illustrated for two representative histological slices in figures 3 & 4. Most bone tissue identified in the histological image (Van Gieson staining, in red in figures 3a and 4a) was also present in the corresponding neutron image (figures 3b and 4b) as illustrated by the high values of the histological fit ratio *Fit$_H$* with an average of 95.0% ± 1.4%. In the registered images (figures 3c and 4c), very few "green" pixels (corresponding to the segmented bone pixels remaining unmatched from the histological image) can be observed. However, the average neutron fit ratio *Fit$_N$* of 75.1% ± 7.0% revealed that the neutron images contained more segmented tissues than their histological reference. This result can also be visually observed through the higher content of residual *Bone$_N$* (in fuchsia in figures 3c and 4c).

Stevenel's blue staining (figures 3d and 4d) revealed the presence of soft tissues, structured in filaments (arrows in figure 3d), and as well as thicker tissues (figure 4d), in variable amounts depending on the specimens. A visual comparison between these Stevenel's blue stained histological slices and the corresponding non-segmented neutron images (figures 3b and 4b) revealed that, in addition to mineralised bone tissue, neutron tomography is sensitive to soft tissues, appearing as brighter pixels. Residual tissues in the segmented neutron images (fuchsia in figures 3c and 4c), left unmatched after the image registration procedure, were also visually associated with soft tissues through a comparison with Stevenel's blue stained histological slices.

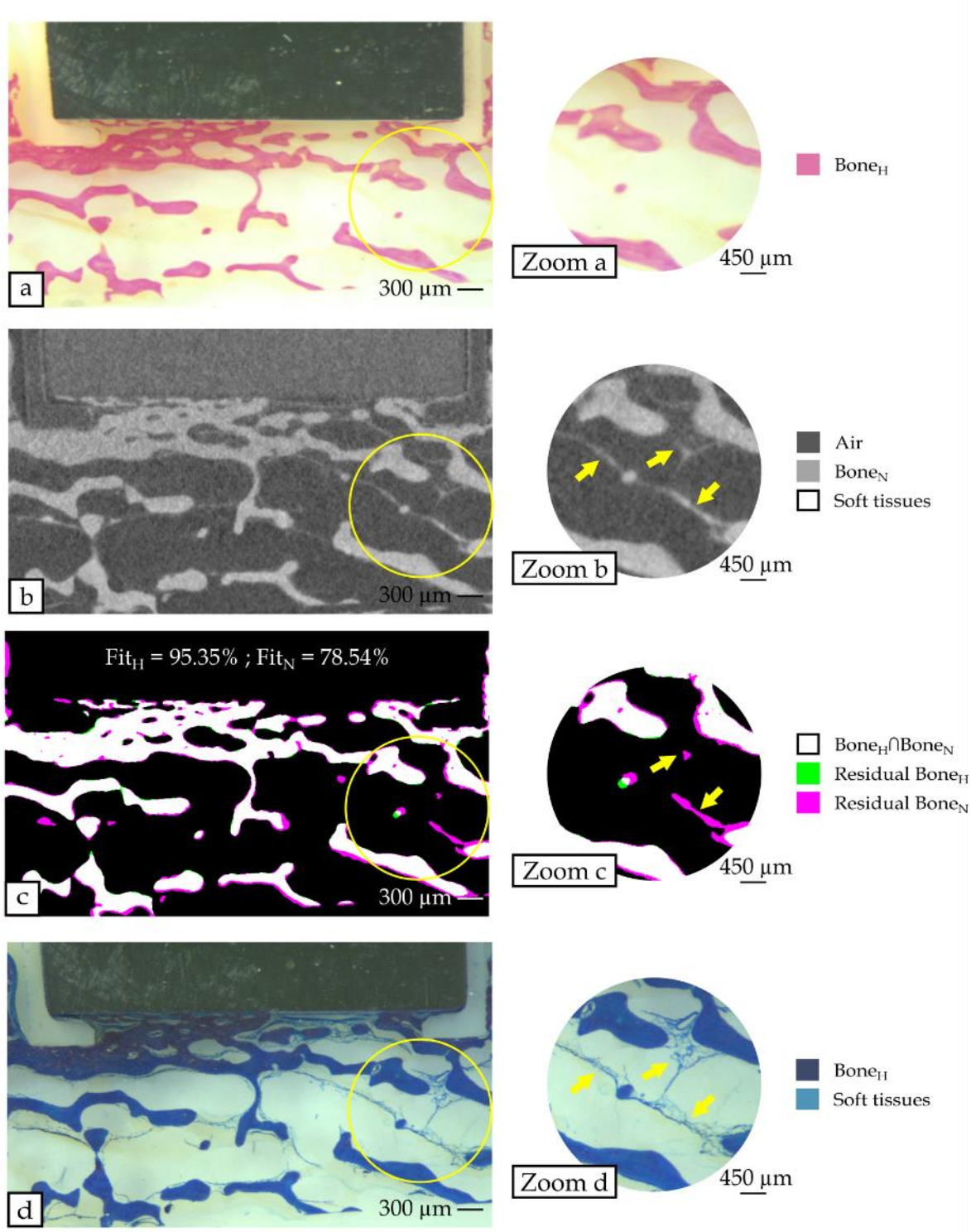

Figure 3: Comparison of representative histological slices to the corresponding neutron image. (a) Histological slice of a specimen after Van Gieson staining, colouring mineralised bone tissue in red. (b) Corresponding non-segmented neutron image, identified after image registration. (c) Result after registering (a) to (b) with corresponding Fit_H and Fit_N ratios. Overlapping segmented bone pixels are displayed in white, residual bone pixels left in the segmented histological image in green and those left in the segmented neutron image in fuchsia. (d) Histological slice stained with Stevenel's blue, where non-mineralised soft tissues appear as light blue. In the zooms (yellow circles), the arrows point at tissues not coloured after Van Gieson staining (a), composed of brighter pixels in the neutron image (b), and identified as non-mineralised soft tissues (d).

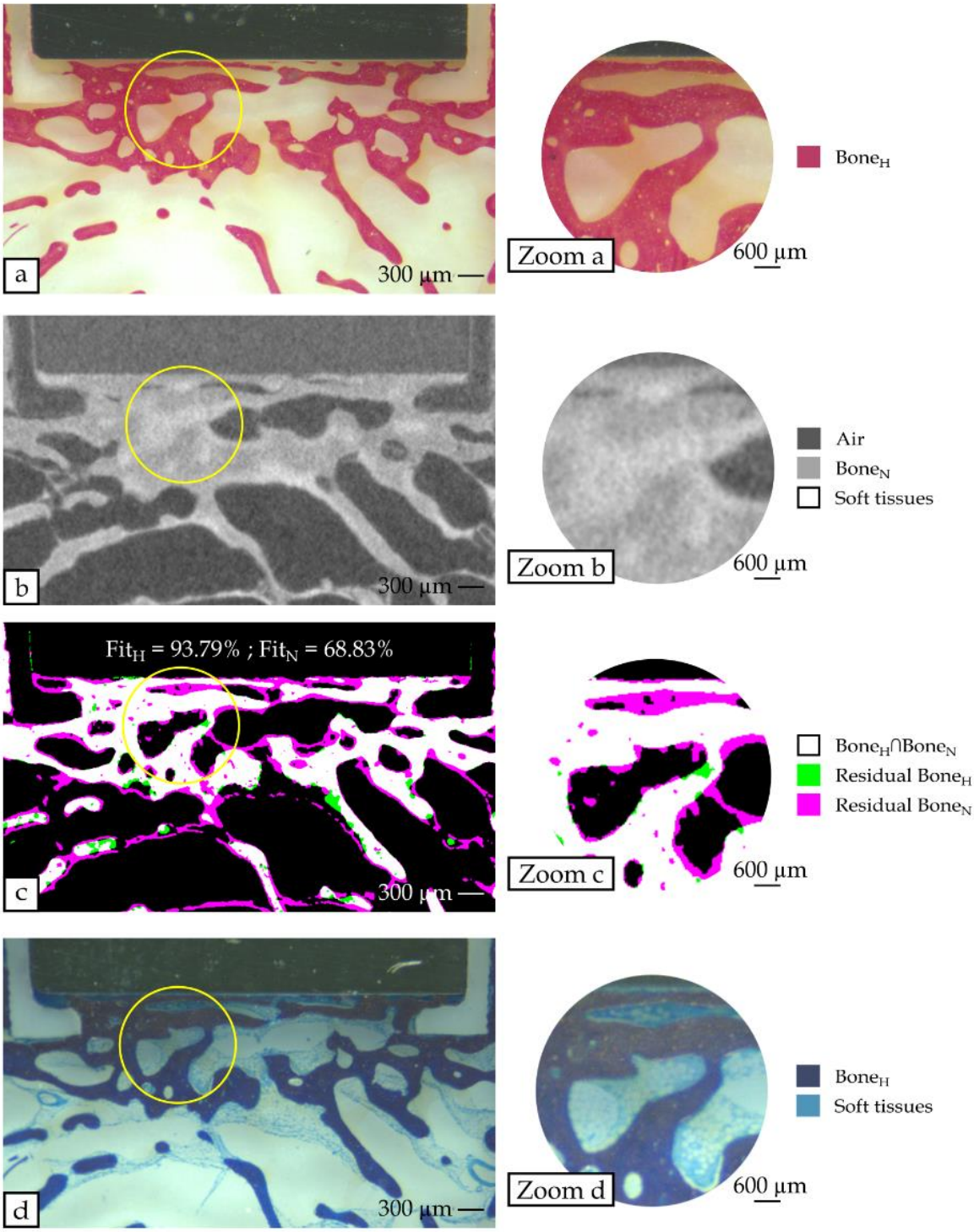

Figure 4: Comparison of representative histological slice to the corresponding neutron image with large amount of soft tissue. (a) Histological slice of a specimen after Van Gieson staining, colouring mineralised bone tissue in red. (b) Corresponding non-segmented neutron image, identified after image registration. On the right, the zoom (yellow circle) highlights a region with a large proportion of soft tissues, associated with brighter pixels. (c) Result after registering (a) to (b) with corresponding Fit_H and Fit_N ratios. (d) Histological slice stained with Stevenel's blue where non-mineralised soft tissues appear as light blue. It should be noted that the pixels in the segmented neutron image (fuchsia, (c)), which are not visible in (a), appear to correspond to soft tissues which could not be accurately segmented out but are visible from (d), and which results in the low Fit_N ratio.

The linear regression analysis indicated a significant correlation between the two modalities for both *BIC* ratios ($R = 0.77$, $p = 0.0034$) and bone content ($R = 0.89$, $p = 0.0001$) (figure 5). Values of the *BIC* ratio and of the bone content were systematically higher when measured in the neutron images compared to the histological images, which can be explained by the simultaneous detection of bone and soft tissues in the neutron images (white and fuchsia pixels in figures 3c and 4c). The values of the *BIC* ratio extracted from the histological and neutrons images were 47.2 % ± 16.8 % and 70.6 % ± 15.5 %, respectively. The bone content reached 42.2 % ± 11.3 % in the histological slices and 53.1 % ± 13.0 % in the neutron images.

4. Discussion

Recent works highlighted that neutron tomography is a promising alternative to X-rays tomography for the investigation of the bone-implant interface, thanks to the absence of metal artefacts (Isaksson et al., 2017; Le Cann et al., 2017). The originality of the present study is to evaluate the ability of neutron tomography to study the bone-implant interface, and quantitatively compare it to histology, a gold standard technique in bone-implant research. A standardised implant model with a bone chamber was analysed using both techniques and a 1:1 comparison was performed after registering the images acquired with these two modalities.

This image registration was obtained by maximising the sum of two fit ratios, Fit_H and Fit_N, which evaluate the pixel correspondence between modalities, while varying their relative position and orientation. The high values of the histological fit ratio (Fit_H) suggested that no better match containing all the bone tissue included in the histological slice could be found in the neutron image volume. Moreover, a significant correlation was found between histological and neutron evaluations of the *BIC* ratio and bone content in the bone chamber. These results confirmed that neutron tomography can be used to retrieve information on bone tissue in the vicinity of metal implants, as previously observed (Isaksson et al., 2017; Le Cann et al., 2017).

The lower values of the neutron fit ratio (Fit_N) indicated that neutron images contained more information about biological tissues than histology, and thus that neutron tomography is sensitive to other tissues, in addition to bone tissue. The neutron image volumes presented brighter areas, identified as soft tissue by comparison with the Stevenel's blue colouration of the histological slices (figures 3 and 4). Therefore, the use of a single correlation coefficient to evaluate the quality of the registration, as commonly implemented in the literature (Geng et al., 2016; Turgeon et al., 2005; Vermandel et al., 2007), appears to be limited to assess the performance of the registration method when comparing images containing different information.

The threshold-based segmentation procedure attempting to remove soft tissues from the neutrons images was found to be not completely effective, as illustrated by the unmatched tissues after registration (fuchsia pixels in figure 3c and figure 4c). This can be explained by the slight arbitrariness in the choice to use a fixed upper threshold for all images in the proposed technique. The additional tissues led to an overestimation of the *BIC* ratio (23%) and the bone content (11%) when calculated from the neutron images as compared to histology. The larger overestimation of the *BIC* ratio might be due to the smaller region used in the calculation (only the implant surface line), while bone content was estimated from the full surface region of the implant bone chamber. Neutron tomography applied to biological pearls already highlighted its ability to identify collagenous material (Micieli et al., 2018). The non-mineralised tissues stained with Stevenel's blue in bone specimens may correspond to bone marrow

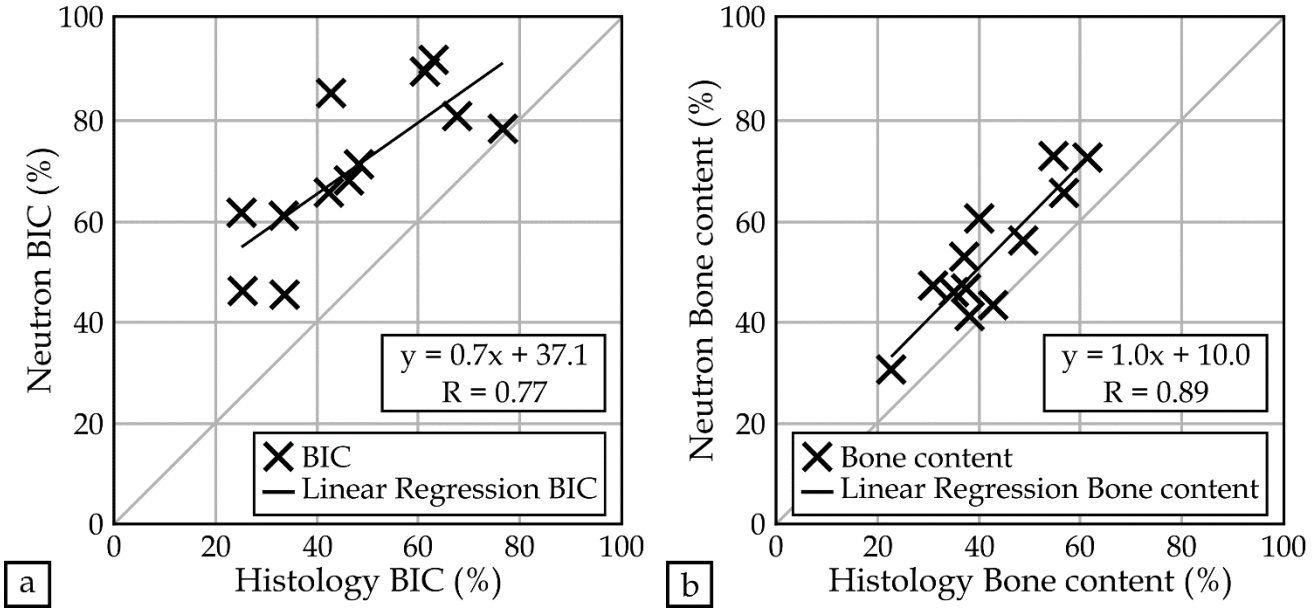

Figure 5: Variation of the *BIC* ratio (a) and bone content (b) as obtained with the histological and neutron images. A linear regression analysis was performed between the two modalities for both parameters.

and/or fibrous tissues (Rustom et al., 2016) and their presence could explain the additional regions observed in the neutron volume images. Bone marrow has a high hydrogen content and fibrous tissues are made of collagenous material, which were both reported to have a higher neutron attenuation than hydroxyapatite, the main component of mineralised bone tissue (Sołtysiak et al., 2018). So far, neutron tomography has only been sporadically applied to bone research (Isaksson et al., 2017; Le Cann et al., 2017) and the ability to distinguish mineralised from soft tissues at high resolution has not been thoroughly investigated yet. Studying non-mineralised soft tissue during osseointegration is of interest since bone formation and remodelling passes through a collagenous material deposition phase before mineralisation of the bone tissue (Davies, 1996), and remnants of fibrous tissues along healing could be an indicator of a failed osseointegration (Haïat et al., 2014). Further work is required to deepen this analysis, since soft tissue content is also related to animal model and anatomical location (Kuzyk and Schemitsch, 2011; Li et al., 2019).

To ensure a good neutron image quality, the bone specimens were dried before being imaged, which allowed the reduction of the overall attenuation associated with high-hydrogen content (Schwarz et al., 2005), as well as maximised image stability along the scan. Former studies performed with comparable specimens (Isaksson et al., 2017; Le Cann et al., 2017) proposed an immersion in heavy water (D_2O or deuterium oxide), where hydrogen atoms are replaced by their isotope deuterium, which has a lower attenuation to neutrons. However, proper H_2O/D_2O exchange as well as adequate humidity control are still cumbersome to obtain, and achieving a systematic suitable image quality is complex (Le Cann et al., 2017). Imaging dried specimens was therefore adopted here, to provide optimal contrast between structures within the bone cores. As drying condensed the soft tissues, their hydrogen content was concentrated in smaller volumes, which locally induced a higher attenuation of neutrons. Hence, soft tissues appeared with higher grey values in the reported neutron images compared to bone. However, the PMMA embedding process for histology included a preparation phase of soaking into liquids, which likely has heterogeneously affected the soft tissues. When comparing neutron images to histological images, some soft tissues appeared thicker after Stevenel's blue staining (figure 4d) while others kept a similar structure as in the neutron scans (figure 3d). Further analyses are required to define an adequate preservation protocol. Additionally, to increase contrast in the neutron images, contrast agents could be used, such as isotopes sensitivity often adopted in plant research (Tötzke et al., 2017), or charged ions as employed in batteries (Owejan et al., 2012).

Differentiation of mineralised and soft tissues was also affected by the signal-to-noise ratio of the neutron images, which could be further improved both in terms of acquisition parameters and in terms of the ensuing image analysis. For instance, different image analysis strategies could be adopted, such as dual-histogram analysis as an alternative registration procedure (Stamati et al., 2020). In recent years, remarkable advances in neutron imaging in terms of resolution and duration of the scans were made available (Hussey et al., 2017; Tengattini et al., 2020), and further improvements are expected in the future. For example, through the implementation of enhanced detectors, the pixel size adopted here was reduced to 7.5 µm compared to 23 µm (Le Cann et al., 2017) or 13.5 µm (Isaksson et al., 2017) in previous studies.

In addition to the possible technical improvements discussed above, this study is based on four bone-implant specimens coming from one single animal. Nonetheless, the coin-shaped implant model has been validated in former studies, revealing comparable bone content and *BIC* values as quantified by histological slices after 13 weeks of healing (Fraulob et al., 2020a; Le Cann et al., 2020; Mathieu et al., 2011; Vayron et al., 2014).

5. Conclusion

In this work, a quantitative comparison of neutron tomography to histological analysis was performed in the investigation of the bone-implant interface, with the aim to assess neutron sensitivity to biological tissues. This study confirmed the ability of neutron tomography to obtain high resolution images of bone tissue close to a metallic implant , without the typical artefacts observed with the more frequently adopted X-ray tomography, while retaining the non-destructive and 3D nature of the latter. In addition, the potential of neutron tomography for the identification of soft tissues within the bone network was highlighted, which might prove to be beneficial for the capacity to study key bone architectural results. Further work is required to optimise image contrast and enhance the process adopted for the differentiation of tissues when using neutron tomography, to complement the investigation of bone and the osseointegration phenomenon. Such enhancements could be further aided by adapted specimen preparation techniques, the ongoing improvements in the acquisition process, as well as development of novel image analysis techniques.

Acknowledgments

This project has received funding from the European Union's Horizon 2020 research, the innovation programme under the Marie Sklodowska-Curie grant agreement No 797764 and from the International Resarch Project (IRP) "Laboratoire Franco-Canadien de Recherches Ultrasonores" (LAFCUS). In addition, this project has received funding from the European Research Council (ERC) under the European Union's Horizon 2020 research and innovation program (grant agreement No 682001, project ERC Consolidator Grant 2015 BoneImplant). The authors want to acknowledge the Institut Laue-Langevin, Grenoble, France for providing the beamtime at the NeXT beamline (https://doi.ill.fr/10.5291/ILL-DATA.UGA-81) and would like to thank Nicolas Lenoir for assistance.

Conflicts of interest

The authors declare that they have no conflict of interest.

References

Berglundh, T., Abrahamsson, I., Lang, N.P., Lindhe, J., 2003. De novo alveolar bone formation adjacent to endosseous implants. Clinical Oral Implants Research 14, 251–262. https://doi.org/10.1034/j.1600-0501.2003.00972.x

Bissinger, O., Probst, F.A., Wolff, K.-D., Jeschke, A., Weitz, J., Deppe, H., Kolk, A., 2017. Comparative 3D micro-CT and 2D histomorphometry analysis of dental implant osseointegration in the maxilla of minipigs. Journal of Clinical Periodontology 44, 418–427. https://doi.org/10.1111/jcpe.12693

Burca, G., Nagella, S., Clark, T., Tasev, D., Rahman, I.A., Garwood, R.J., Spencer, A.R.T., Turner, M.J., Kelleher, J.F., 2018. Exploring the potential of neutron imaging for life sciences on IMAT. Journal of Microscopy 272, 242–247. https://doi.org/10.1111/jmi.12761

Burghardt, A.J., Link, T.M., Majumdar, S., 2011. High-resolution Computed Tomography for Clinical Imaging of Bone Microarchitecture. Clinical Orthopaedics and Related Research® 469, 2179–2193. https://doi.org/10.1007/s11999-010-1766-x

Cekanova, M., Donnell, R., Bilheux, H., Bilheux, J.-Ch., 2014. Neutron imaging: Detection of cancer using animal model, in: Proceedings of the 2014 Biomedical Sciences and Engineering Conference. IEEE, pp. 1–4. https://doi.org/10.1109/BSEC.2014.6867752

Chevallier, N., Anagnostou, F., Zilber, S., Bodivit, G., Maurin, S., Barrault, A., Bierling, P., Hernigou, P., Layrolle, P., Rouard, H., 2010. Osteoblastic differentiation of human mesenchymal stem cells with platelet lysate. Biomaterials 31, 270–278. https://doi.org/10.1016/j.biomaterials.2009.09.043

Davies, J.E., 1996. In vitro modeling of the bone/implant interface. The Anatomical Record 245, 426–445. https://doi.org/10.1002/(SICI)1097-0185(199606)245:2<426::AID-AR21>3.0.CO;2-Q

De Smet, E., Jaecques, S.V.N., Wevers, M., Jansen, J.A., Jacobs, R., Sloten, J. Vander, Naert, I.E., 2006. Effect of controlled early implant loading on bone healing and bone mass in guinea pigs, as assessed by micro-CT and histology. European Journal of Oral Sciences 114, 232–242. https://doi.org/10.1111/j.1600-0722.2006.00355.x

Eskelinen, A., Remes, V., Helenius, I., Pulkkinen, P., Nevalainen, J., Paavolainen, P., 2006. Uncemented total hip arthroplasty for primary osteoarthritis in young patients: A mid-to long-term follow-up study from the Finnish Arthroplasty Register. Acta Orthopaedica 77, 57–70. https://doi.org/10.1080/17453670610045704

Fraulob, M., Le Cann, S., Voumard, B., Yasui, H., Yano, K., Vayron, R., Matsukawa, M., Zysset, P., Haïat, G., 2020a. Multimodal Evaluation of the Spatiotemporal Variations of Periprosthetic Bone Properties. Journal of Biomechanical Engineering 142, 1–34. https://doi.org/10.1115/1.4048399

Fraulob, M., Pang, S., Le Cann, S., Vayron, R., Laurent-Brocq, M., Todatry, S., Soares, J.A.N.T., Jasiuk, I., Haïat, G., 2020b. Multimodal characterization of the bone-implant interface using Raman spectroscopy and nanoindentation. Medical Engineering & Physics 84, 60–67. https://doi.org/10.1016/j.medengphy.2020.07.013

Geng, H., Todd, N.M., Devlin-Mullin, A., Poologasundarampillai, G., Kim, T.B., Madi, K., Cartmell, S., Mitchell, C.A., Jones, J.R., Lee, P.D., 2016. A correlative imaging based methodology for accurate quantitative assessment of bone formation in additive manufactured implants. Journal of Materials Science: Materials in Medicine 27, 112. https://doi.org/10.1007/s10856-016-5721-6

Gielkens, P.F.M., Schortinghuis, J., de Jong, J.R., Huysmans, M.C.D.N.J.M., Leeuwen, M.B.M. Van, Raghoebar, G.M., Bos, R.R.M., Stegenga, B., 2008. A comparison of micro-CT, microradiography and histomorphometry in bone research. Archives of Oral Biology 53, 558–566. https://doi.org/10.1016/j.archoralbio.2007.11.011

Haïat, G., Wang, H.-L., Brunski, J., 2014. Effects of Biomechanical Properties of the Bone–Implant Interface on Dental Implant Stability: From In Silico Approaches to the Patient's Mouth. Annual Review of Biomedical Engineering 16, 187–213. https://doi.org/10.1146/annurev-bioeng-071813-104854

Henke, M., Junker, A., Neumann, K., Altmann, T., Gladilin, E., 2019. Comparison and extension of three methods for automated registration of multimodal plant images. Plant Methods 15, 44. https://doi.org/10.1186/s13007-019-0426-8

Hussey, D.S., LaManna, J.M., Baltic, E., Jacobson, D.L., 2017. Neutron imaging detector with 2 μm spatial resolution based on event reconstruction of neutron capture in gadolinium oxysulfide scintillators. Nuclear Instruments and Methods in Physics Research Section A: Accelerators, Spectrometers, Detectors and Associated Equipment 866, 9–12. https://doi.org/10.1016/j.nima.2017.05.035

Isaksson, H., Le Cann, S., Perdikouri, C., Turunen, M.J., Kaestner, A., Tägil, M., Hall, S.A., Tudisco, E., 2017. Neutron tomographic imaging of bone-implant interface: Comparison with X-ray tomography. Bone 103, 295–301. https://doi.org/10.1016/j.bone.2017.07.022

Jackson, N., Assad, M., Vollmer, D., Stanley, J., Chagnon, M., 2019. Histopathological Evaluation of Orthopedic Medical Devices: The State-of-the-art in Animal Models, Imaging, and Histomorphometry Techniques. Toxicologic Pathology 47, 280–296. https://doi.org/10.1177/0192623318821083

Jimbo, R., Anchieta, R., Baldassarri, M., Granato, R., Marin, C., Teixeira, H.S., Tovar, N., Vandeweghe, S., Janal, M.N., Coelho, P.G., 2013. Histomorphometry and Bone Mechanical Property Evolution Around Different Implant Systems at Early Healing Stages.

Implant Dentistry 22, 596–603. https://doi.org/10.1097/ID.0b013e31829f1f4b

Kardjilov, N., Manke, I., Woracek, R., Hilger, A., Banhart, J., 2018. Advances in neutron imaging. Materials Today 21, 652–672. https://doi.org/10.1016/j.mattod.2018.03.001

Kovacs, D.G., Rechner, L.A., Appelt, A.L., Berthelsen, A.K., Costa, J.C., Friborg, J., Persson, G.F., Bangsgaard, J.P., Specht, L., Aznar, M.C., 2018. Metal artefact reduction for accurate tumour delineation in radiotherapy. Radiotherapy and Oncology 126, 479–486. https://doi.org/10.1016/j.radonc.2017.09.029

Kurtz, S.M., Ong, K.L., Lau, E., Bozic, K.J., 2014. Impact of the Economic Downturn on Total Joint Replacement Demand in the United States. The Journal of Bone and Joint Surgery-American Volume 96, 624–630. https://doi.org/10.2106/JBJS.M.00285

Kurtz, S.M., Ong, K.L., Schmier, J., Mowat, F., Saleh, K., Dybvik, E., Kärrholm, J., Garellick, G., Havelin, L.I., Furnes, O., Malchau, H., Lau, E., 2007. Future Clinical and Economic Impact of Revision Total Hip and Knee Arthroplasty. The Journal of Bone & Joint Surgery 89, 144–151. https://doi.org/10.2106/JBJS.G.00587

Kuzyk, P., Schemitsch, E., 2011. The basic science of peri-implant bone healing. Indian Journal of Orthopaedics 45, 108. https://doi.org/10.4103/0019-5413.77129

Le Cann, S., Törnquist, E., Silva Barreto, I., Fraulob, M., Albini Lomami, H., Verezhak, M., Guizar-Sicairos, M., Isaksson, H., Haïat, G., 2020. Spatio-temporal evolution of hydroxyapatite crystal thickness at the bone-implant interface. Acta Biomaterialia 116, 391–399. https://doi.org/10.1016/j.actbio.2020.09.021

Le Cann, S., Tudisco, E., Perdikouri, C., Belfrage, O., Kaestner, A., Hall, S., Tägil, M., Isaksson, H., 2017. Characterization of the bone-metal implant interface by Digital Volume Correlation of in-situ loading using neutron tomography. Journal of the Mechanical Behavior of Biomedical Materials 75, 271–278. https://doi.org/10.1016/j.jmbbm.2017.07.001

Li, J.Y., Pow, E.H.N., Zheng, L.W., Ma, L., Kwong, D.L.W., Cheung, L.K., 2014. Quantitative analysis of titanium-induced artifacts and correlated factors during micro-CT scanning. Clinical Oral Implants Research 25, 506–510. https://doi.org/10.1111/clr.12200

Li, Y., Meng, Y., Yu, X., 2019. The Unique Metabolic Characteristics of Bone Marrow Adipose Tissue. Frontiers in Endocrinology 10, 1–13. https://doi.org/10.3389/fendo.2019.00069

Markelj, P., Tomaževič, D., Likar, B., Pernuš, F., 2012. A review of 3D/2D registration methods for image-guided interventions. Medical Image Analysis 16, 642–661. https://doi.org/10.1016/j.media.2010.03.005

Mathieu, V., Fukui, K., Matsukawa, M., Kawabe, M., Vayron, R., Soffer, E., Anagnostou, F., Haiat, G., 2011. Micro-Brillouin Scattering Measurements in Mature and Newly Formed Bone Tissue Surrounding an Implant. Journal of Biomechanical Engineering 133, 1–6. https://doi.org/10.1115/1.4003131

Mathieu, V., Vayron, R., Soffer, E., Anagnostou, F., Haïat, G., 2012. Influence of Healing Time on the Ultrasonic Response of the Bone-Implant Interface. Ultrasound in Medicine & Biology 38, 611–618. https://doi.org/10.1016/j.ultrasmedbio.2011.12.014

McLaughlin, R.A., Hipwell, J., Hawkes, D.J., Noble, J.A., Byrne, J. V., Cox, T.C., 2005. A comparison of a similarity-based and a feature-based 2-D-3-D registration method for neurointerventional use. IEEE Transactions on Medical Imaging 24, 1058–1066. https://doi.org/10.1109/TMI.2005.852067

Meagher, M.J., Parwani, R.N., Virdi, A.S., Sumner, D.R., 2017. Optimizing a micro-computed tomography-based surrogate measurement of bone-implant contact. Journal of Orthopaedic Research 176, 139–148. https://doi.org/10.1002/jor.23716

Meijering, E.H.W., Niessen, W.J., Viergever, M.A., 2001. Quantitative evaluation of convolution-based methods for medical image interpolation. Medical Image Analysis 5, 111–126. https://doi.org/10.1016/S1361-8415(00)00040-2

Micieli, D., Di Martino, D., Musa, M., Gori, L., Kaestner, A., Bravin, A., Mittone, A., Navone, R., Gorini, G., 2018. Characterizing pearls structures using X-ray phase-contrast and neutron imaging: a pilot study. Scientific Reports 8, 12118. https://doi.org/10.1038/s41598-018-30545-z

Moy, P.K., Medina, D., Shetty, V., Aghaloo, T.L., 2005. Dental implant failure rates and associated risk factors. The International journal of oral & maxillofacial implants 20, 569–77.

Neldam, C.A., Sporring, J., Rack, A., Lauridsen, T., Hauge, E.-M., Jørgensen, H.L., Jørgensen, N.R., Feidenhansl, R., Pinholt, E.M., 2017. Synchrotron radiation μCT and histology evaluation of bone-to-implant contact. Journal of Cranio-Maxillofacial Surgery 45, 1448–1457. https://doi.org/10.1016/j.jcms.2017.05.019

Ollion, J., Cochennec, J., Loll, F., Escudé, C., Boudier, T., 2013. TANGO: a generic tool for high-throughput 3D image analysis for studying nuclear organization. Bioinformatics 29, 1840–1841. https://doi.org/10.1093/bioinformatics/btt276

Owejan, J.P., Gagliardo, J.J., Harris, S.J., Wang, H., Hussey, D.S., Jacobson, D.L., 2012. Direct measurement of lithium transport in graphite electrodes using neutrons. Electrochimica Acta 66, 94–99. https://doi.org/10.1016/j.electacta.2012.01.047

Palmquist, A., 2018. A multiscale analytical approach to evaluate osseointegration. Journal of Materials Science: Materials in Medicine 29, 60. https://doi.org/10.1007/s10856-018-6068-y

R Development Core Team, 2005. R: A language and environment for statistical computing., in: R Foundation for Statistical Computing. Vienna, Austria.

Ridler, T.W., Calvard, S., 1978. Picture Thresholding Using an Iterative Selection Method. IEEE Transactions on Systems, Man, and Cybernetics 8, 630–632. https://doi.org/10.1109/TSMC.1978.4310039

Rønold, H.J., Ellingsen, J.E., 2002. Effect of micro-roughness produced by TiO2 blasting—tensile testing of bone attachment by using coin-shaped implants. Biomaterials 23, 4211–4219. https://doi.org/10.1016/S0142-9612(02)00167-9

Rønold, H.J., Lyngstadaas, S.P., Ellingsen, J.E., 2003. Analysing the optimal value for titanium implant roughness in bone attachment using a tensile test. Biomaterials 24, 4559–4564. https://doi.org/10.1016/S0142-9612(03)00256-4

Rustom, L.E., Boudou, T., Lou, S., Pignot-Paintrand, I., Nemke, B.W., Lu, Y., Markel, M.D., Picart, C., Wagoner Johnson, A.J., 2016. Micropore-induced capillarity enhances bone distribution in vivo in biphasic calcium phosphate scaffolds. Acta Biomaterialia 44, 144–154. https://doi.org/10.1016/j.actbio.2016.08.025

Schindelin, J., Arganda-Carreras, I., Frise, E., Kaynig, V., Longair, M., Pietzsch, T., Preibisch, S., Rueden, C., Saalfeld, S., Schmid, B., Tinevez, J.-Y., White, D.J., Hartenstein, V., Eliceiri, K., Tomancak, P., Cardona, A., 2012. Fiji: an open-source platform for biological-image analysis. Nature Methods 9, 676–682. https://doi.org/10.1038/nmeth.2019

Schwarz, D., Vontobel, P., Lehmann, E.H., Meyer, C.A., Bongartz, G., 2005. Neutron tomography of internal structures of vertebrate remains: A comparison with X-ray computed tomography. Palaeontologia Electronica 8.

Sharkey, P.F., Lichstein, P.M., Shen, C., Tokarski, A.T., Parvizi, J., 2014. Why Are Total Knee Arthroplasties Failing Today—Has Anything Changed After 10 Years? The Journal of Arthroplasty 29, 1774–1778. https://doi.org/10.1016/j.arth.2013.07.024

Shemtov-Yona, K., Rittel, D., 2015. An Overview of the Mechanical Integrity of Dental Implants. BioMed Research International 2015, 1–11. https://doi.org/10.1155/2015/547384

Soffer, E., Ouhayoun, J.P., Meunier, A., Anagnostou, F., 2006. Effects of autologous platelet lysates on ceramic particle resorption and new bone formation in critical size defects: The role of anatomical sites. Journal of Biomedical Materials Research Part B: Applied Biomaterials 79B, 86–94. https://doi.org/10.1002/jbm.b.30516

Sołtysiak, A., Miśta-Jakubowska, E.A., Dorosz, M., Kosiński, T., Fijał-Kirejczyk, I., 2018. Estimation of collagen presence in dry bone using combined X-ray and neutron radiography. Applied Radiation and Isotopes 139, 141–145. https://doi.org/10.1016/j.apradiso.2018.03.024

Stalder, A.K., Ilgenstein, B., Chicherova, N., Deyhle, H., Beckmann, F., Müller, B., Hieber, S.E., 2014. Combined use of micro computed tomography and histology to evaluate the regenerative capacity of bone grafting materials. International Journal of Materials Research 105, 679–691. https://doi.org/10.3139/146.111050

Stamati, O., Andò, E., Roubin, E., Cailletaud, R., Wiebicke, M., Pinzon, G., Couture, C., Hurley, R., Caulk, R., Caillerie, D., Matsushima, T., Bésuelle, P., Bertoni, F., Arnaud, T., Laborin, A., Rorato, R., Sun, Y., Tengattini, A., Okubadejo, O., Colliat, J.-B., Saadatfar, M., Garcia, F., Papazoglou, C., Vego, I., Brisard, S., Dijkstra, J., Birmpilis, G., 2020. spam: Software for Practical Analysis of Materials. Journal of Open Source Software 5, 2286. https://doi.org/10.21105/joss.02286

Tengattini, A., Lenoir, N., Andò, E., Giroud, B., Atkins, D., Beaucour, J., Viggiani, G., 2020. NeXT-Grenoble, the Neutron and X-ray tomograph in Grenoble. Nuclear Instruments and Methods in Physics Research Section A: Accelerators, Spectrometers, Detectors and Associated Equipment 968, 163939. https://doi.org/10.1016/j.nima.2020.163939

Tengattini, A., Lenoir, N., Andò, E., Viggiani, G., 2021. Neutron imaging for geomechanics: A review. Geomechanics for Energy and the Environment, Deformation Characteristics of Geomaterials – selected papers for 7th International Symposium, IS-Glasgow2019 27, 100206. https://doi.org/10.1016/j.gete.2020.100206

Tötzke, C., Kardjilov, N., Manke, I., Oswald, S.E., 2017. Capturing 3D Water Flow in Rooted Soil by Ultra-fast Neutron Tomography. Scientific Reports 7, 6192. https://doi.org/10.1038/s41598-017-06046-w

Treece, G., 2017. Refinement of clinical X-ray computed tomography (CT) scans containing metal implants. Computerized Medical Imaging and Graphics 56, 11–23. https://doi.org/10.1016/j.compmedimag.2017.01.005

Turgeon, G.-A., Lehmann, G., Guiraudon, G., Drangova, M., Holdsworth, D., Peters, T., 2005. 2D-3D registration of coronary angiograms for cardiac procedure planning and guidance. Medical Physics 32, 3737–3749. https://doi.org/10.1118/1.2123350

Urciuoli, A., Zanolli, C., Fortuny, J., Almécija, S., Schillinger, B., Moyà-Solà, S., Alba, D.M., 2018. Neutron-based computed microtomography: Pliobates cataloniae and Barberapithecus huerzeleri as a test-case study. American Journal of Physical Anthropology 166, 987–993. https://doi.org/10.1002/ajpa.23467

Vayron, R., Barthel, E., Mathieu, V., Soffer, E., Anagnostou, F., Haiat, G., 2012. Nanoindentation Measurements of Biomechanical Properties in Mature and Newly Formed Bone Tissue Surrounding an Implant. Journal of Biomechanical Engineering 134, 1–6. https://doi.org/10.1115/1.4005981

Vayron, R., Barthel, E., Mathieu, V., Soffer, E., Anagnostou, F., Haiat, G., 2011. Variation of biomechanical properties of newly formed bone tissue determined by nanoindentation as a function of healing time. Computer Methods in Biomechanics and Biomedical Engineering 14, 139–140. https://doi.org/10.1080/10255842.2011.593770

Vayron, R., Matsukawa, M., Tsubota, R., Mathieu, V., Barthel, E., Haiat, G., 2014. Evolution of bone biomechanical properties at the micrometer scale around titanium implant as a function of healing time. Physics in Medicine and Biology 59, 1389–1406. https://doi.org/10.1088/0031-9155/59/6/1389

Vermandel, M., Betrouni, N., Gauvrit, J., Pasquier, D., Vasseur, C., Rousseau, J., 2007. Intrinsic 2D/3D registration based on a hybrid approach: use in the radiosurgical imaging process. Cellular and molecular biology (Noisy-le-Grand, France) 52, 44–53.

Watkin, K.L., Bilheux, H.Z., Ankner, J.F., 2009. Probing the Potential of Neutron Imaging for Biomedical and Biological Applications. pp. 253–264. https://doi.org/10.1007/978-0-387-78693-3_14

Winter, W., Heckmann, S.M., Weber, H.P., 2004. A time-dependent healing function for immediate loaded implants. Journal of Biomechanics 37, 1861–1867. https://doi.org/10.1016/j.jbiomech.2004.02.033

Wirth, A.J., Goldhahn, J., Flaig, C., Arbenz, P., Müller, R., Van Lenthe, G.H., 2011. Implant stability is affected by local bone microstructural quality. Bone 49, 473–478. https://doi.org/10.1016/j.bone.2011.05.001